

<i>inj</i>	injection
<i>th</i>	throat
<i>cc</i>	closed-closed
<i>max</i>	maximum
<i>vs</i>	vortex shedding
<i>ch</i>	chamber
<i>N</i>	Nozzle
<i>w</i>	working

Abbreviations	
AVS	Angle Vortex Shedding
RSRM	Reusable Solid Rocket Motor
FFT	Fast Fourier Transform
SVS	Surface Vortex Shedding
OVS	Obstacle Vortex Shedding
SRM	Solid Rocket Motor
POA	Pressure Oscillation Analysis

1. INTRODUCTION

In the past 70 years, vortex shedding phenomenon as an origin of aeroacoustic instability inside SRMs has been continuously studied, in connection with oscillatory behaviors of solid rocket motors that were predicted stable by conventional stability methods (Wu & Kung, 2000). The vortex shedding phenomenon is most troublesome for the low order pressure oscillation modes and seems to be important on the evaluation of aeroacoustic instability (Thirumorthy, et al., 2017). Most of the recent studies try to induce the mechanisms for vortex shedding phenomenon in relation to the developments of large segmented solid rocket motors (Ferretti, et al., 2011). Vortex shedding driven oscillations have been observed in motors such as Space Shuttle, Ariane and Titan SRMs (Cosyn, et al., 2005) that have a slender ratio (L/D) between 9-12 (Traineau, et al., 1997), (Prévost, et al., 2005). These SRMs include of segmented cylindrical cases and a submerged nozzle, which a number of thermal protection inhibitors separate them (Anthoine, et al., 2000). Fig. 1 shows the configuration of RSRM's grains and thermal protection inhibitor (McWhorter, et al., 2003).

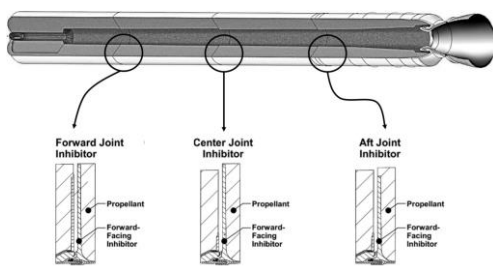


Fig. 1. Configuration of RSRM Grains and Thermal Protection Inhibitor.

Such SRMs exhibit a few tenths of percent pressure, but several percent thrust oscillations on their first longitudinal modes during their working time (Frezzotti, et al., 2018) identified by a frequency close to the motor chamber acoustic modes and the couple with the motor natural modes and make a resonance (Guéry, et al., 2008). Some researchers have presented the dominant factors of acoustic energy in the SRMs and theories on aeroacoustic instabilities (Flandro, et al., 2007). Vortex shedding phenomenon experimentally has been evaluated in the full-scale SRMs and indicated that flow separations due to segmented motors, could increase internal acoustic energy (Culick, 2006). Experiments

demonstrated coupling of the frequencies between the vortex shedding and acoustic modes of the motor (Lee, et al., 2017). As represented in Fig. 2, three kinds of vortex shedding phenomena can be identified in an SRM: OVS, SVS and AVS (Dotson, et al., 1997).

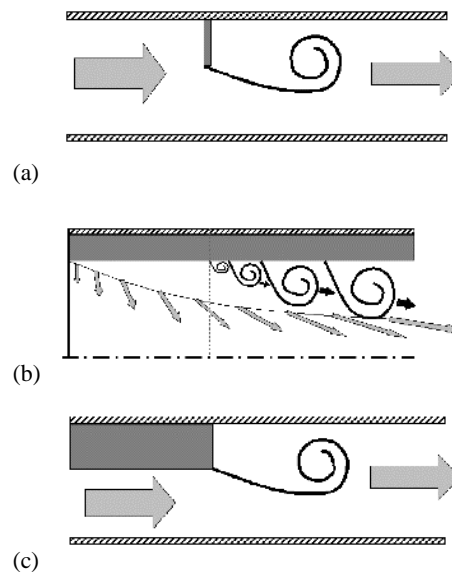


Fig. 2. Three kinds of vortex shedding phenomena; a) OVS, b) SVS and c) AVS.

Aeroacoustic instability can be modeled for complex grains with numerical methods (Javed & Chakraborty, 2015) by solving either steady or unsteady Navier-Stokes equations (Kourta, 1996). Based on these observations, University of Guilan decided to conduct a Ph.D. thesis in mechanical engineering faculty and perform analyzing, simulating and test a series of sub-scaled RSRM to evaluate the role of vortex shedding phenomenon in the aeroacoustic instability.

2. SPACE SRMS AND SUB-SCALED MOTORS

The Space Shuttle consists of two SRMs, burns for 123 s with large amplitude and low frequency thrust oscillations (Mason, et al., 1979). Grain configurations of the Shuttle SRM are shown in Fig. 3(a). Data acquisition from an RSRM static test is shown in Fig. 3(b) and 3(c) (Mason, et al., 2004).

Because of large diameter and length of RSRM, evaluation of its internal ballistic and propellant

Table 1 Effective Parameters on SRM Performance

Variable	Dimension	Descriptions	Variable	Dimension	Descriptions		
1	L_N	L	Nozzle Length	18	r_b	L/s	Burning Rate
2	D_{th}	L	Nozzle Throat Dia.	19	w_b	L	Grain Web
3	D_{ex}	L	Nozzle Exit Dia.	20	V_p	L^3	Propellant Volume
4	P_{ch}	$M/(L * S^2)$	Motor Ave. Pressure	21	\dot{m}_g	M/s	Gas Flow Rate
5	P_{max}	$M/(L * S^2)$	Motor Max. Pressure	22	m_p	M	Propellant Weight
6	t_b	S	Burning Time	23	T_g	T	Gas Temperature
7	t_w	S	Working Time	24	R_g	$L^2/S^2 * T$	Gas Constant
8	L	L	Motor Length	25	γ_g	1	Gas Heat Ratio
9	D	L	Motor Dia.	26	ρ_p	M/L^3	Propellant Density
10	P_{ex}	$M/(L * S^2)$	Nozzle Exit Pressure	27	T_{ini}	T	Initial Temp.
11	V_{ex}	L/s	Nozzle Exit Velocity	28	P_{ini}	$M/(L * S^2)$	Initial Pressure
12	T_{ave}	$M * L/S^2$	Ave. Thrust	29	P_{amb}	$M/(L * S^2)$	Ambient Pressure
13	T_{max}	$M * L/S^2$	Max. Thrust	30	\dot{m}_{ig}	M/s	Igniter Gas Flow Rate
14	I_{total}	$M * L/S$	Total Impulse	31	t_{ig}	S	Igniter Action Time
15	$(I_{sp} * g)$	L/s	Specific Impulse in Gravity	32	$A_{t_{ig}}$	L^2	Igniter Total Exit Area
16	A_b	L^2	Burning Area	33	T_{ig}	T	Igniter Gas Temp.
17	A_p	L^2	Port Area	34	P_{ig}	$M/(L * S^2)$	Igniter Gas Pressure

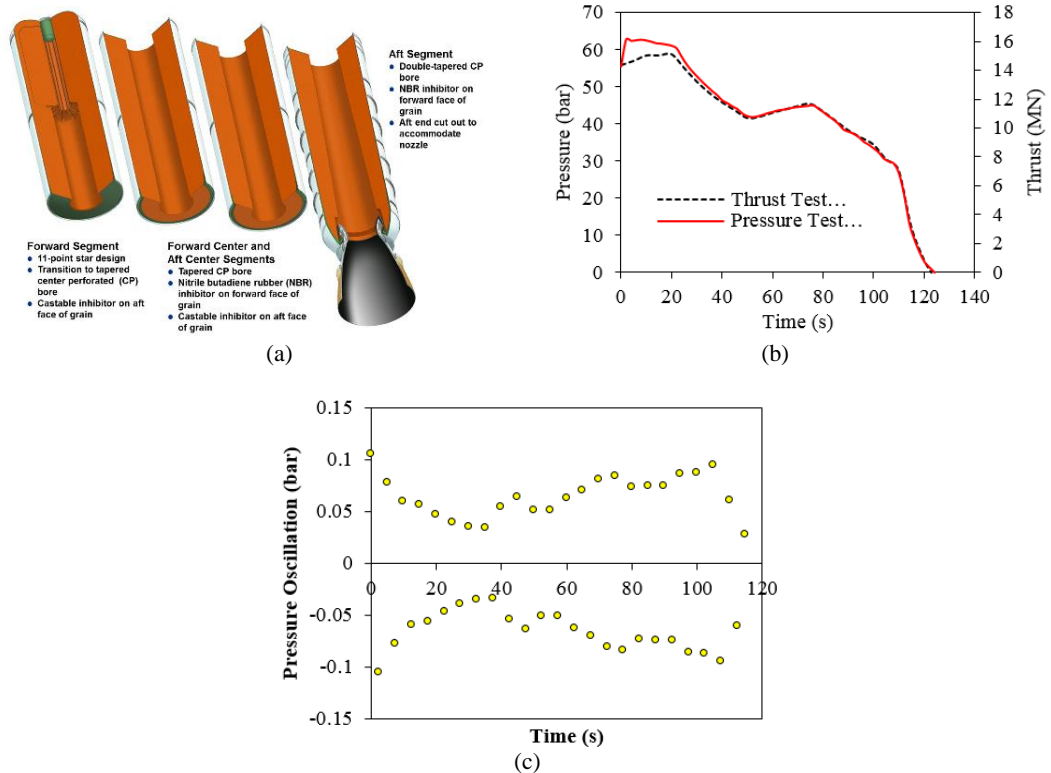


Fig. 3. RSRM: a) Internal Geometry, b) Pressure and Thrust Time History and c) Pressure oscillations.

properties was not economical. So sub-scaled motors such as two types SRTM and MNASA, as shown in Fig. 4, were designed and tested. These motors focus on down selection of material and design changes, analytical model anchoring, etc. (Brown, et al.,

1980). Ariane 5 have three segmented grains with a submerged nozzle, as shown in Fig. 5(a), (Ferretti, et al., 2011) and it's 1:15 sub-scaled solid rocket motor, named LP3, (Fig. 5(b)) was designed and tested to compare with theoretical predictions of full-scaled Ariane 5 (Golafshani & Loh, 1989).

Table 2 Final Result of dimensionless groups obtained from Dimensional Analysis for solid rocket motor

No.	Variable	No.	Variable	No.	Variable	No.	Variable	No.	Variable
1	$\frac{L_N}{D_{th}}$	6	$\frac{t_w}{t_b}$	11	$\frac{T_{max}}{T_{ave}}$	16	$\frac{r_b * t_b}{w_b}$	21	γ_g
2	$\frac{D_{th}}{D}$	7	$\frac{L}{D}$	12	$\frac{I_{total}}{T_{ave} * t_b}$	17	$\frac{w_b}{D}$	22	$\frac{\rho_p * V_p}{m_p}$
3	$\left(\frac{D_{ex}}{D_{th}}\right)^2$	8	$\frac{P_{ex}}{P_{ch}}$	13	$\frac{(I_{sp} * g) * m_p}{I_{total}}$	18	$\frac{V_p}{LD^2}$	23	$\frac{T_{ini}}{T_g}$
4	$\frac{P_{ch}}{\rho_p r_b}$	9	$\frac{V_{ex}}{\sqrt{\gamma_g R_g T_g}}$	14	$\frac{A_b}{D^2}$	19	$\frac{\dot{m}_g}{\rho_p * r_b * A_b}$	24	$\frac{P_{ini}}{P_{amb}}$
5	$\frac{P_{max}}{P_{ch}}$	10	$\frac{T_{ave}}{P_{ch} * D^2}$	15	$\frac{A_p}{D^2}$	20	$\frac{R_g * T_g * \rho_p}{P_{ch}}$	25	$\frac{P_{amb}}{P_{ch}}$
								26	$\frac{\dot{m}_{ig}}{\dot{m}_g}$
								27	$\frac{t_{ig}}{t_b}$
								28	$\frac{A_{t_{ig}}}{A_p}$
								29	$\frac{T_{ig}}{T_g}$
								30	$\frac{P_{ig}}{P_{ini}}$

Table 3 Required Parameters for RSRM Scaling down with the factor of 1:31

Property	Unit	RSRM	Subscale	Property	Unit	RSRM	Subscale
Motor Diameter	mm	3710	119.67	Ave. Chamber Pressure	bar	45	45
Motor Length	mm	38442	1240	Max. Chamber Pressure	bar	54	53
Throat Diameter	mm	1368	44.13	Ave. Thrust	KN	15348.5	16
Nozzle Exit Diameter	mm	3800	122.6	Expansion Ratio	*	7.72	7.72
Action Time	s	123	3.96	Weight	kg	501700	16.84
Burning Time	s	110	3.54	Burning Rate at 43 bar	mm/s	9.347	9.347

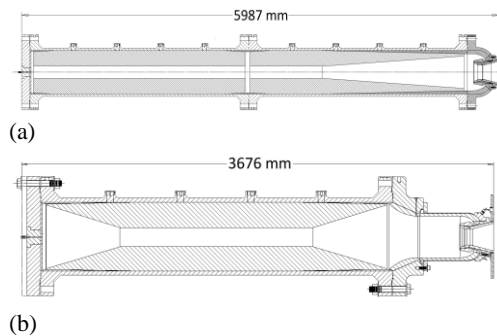


Fig. 4. Subscale a) SRTML and b) MNASA for RSRM Evaluation.

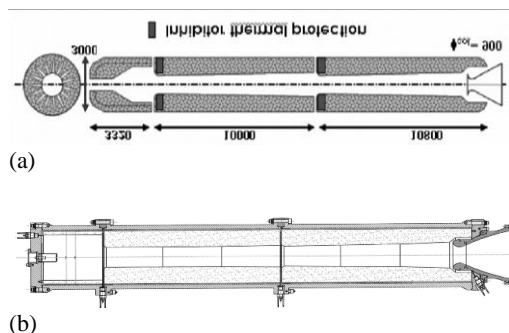


Fig. 5. Ariane 5 SRM: a) Grain schema, b) 1/15 sub-scaled.

3. DESIGN OF SUB-SCALED RSRM

In the design of 1:31 sub-scaled RSRM, dimensionless parameters is generated by the principles of similarity and dimensional analysis (RICHARD, *et al.*, 2007). Ballistic dimensional analyzing for SRMs, at first, all effective parameters should be considered and then using Buckingham's

theorem, the number of dimensionless groups will be determined. Table 1 shows the set of effective parameters for the present work. The number of such parameters is 34 and the number of principle dimensions to the dimensional analysis of these parameters is four. Therefore, according to Buckingham's Theorem, the necessary number of independent groups to the description of this phenomenon is 30. Using this theorem, the result is listed in Table 2.

From the above descriptions and according to designer facilities and purposes, scale downing is done for RSRM with a scale factor of 1:31. Using the Interpretation noted in Table 2, the scaled down parameters obtained as listed in Table 3. Fig. 6 shows 3D modeling and dimensional scheme for subscale motor with outside diameter 122 mm, length 1270 mm and throat diameter 45 mm. The grain geometrical dimensions are 1:31 scale of RSRM.

Predicting the performance of solid rocket motors during the design stage, the burn back steps of the solid propellant should be known (Puskulcu & Ulas, 2008). Fig. 7(a) shows the comparison between full-scale and subscale area regression versus time. Differences observed is due to boundary condition, considered in full-scale and subscale grains. For a majority of the production type's propellants, the most commonly used empirical burning rate equation is $\dot{r} = a(P)^n$ (Seifollahzadeh & Aminian, 2014). Calculating chamber pressure with constant temperature without considering the mass accumulation (Isakari, *et al.*, 2017), conservation relation between the exhausting mass of burning surface and exhausting mass from nozzle gives:

$$\dot{m}_p = \dot{m}_N \Rightarrow \rho_p A_b \dot{r} = \frac{A_t P_c}{c^*} \quad (1)$$

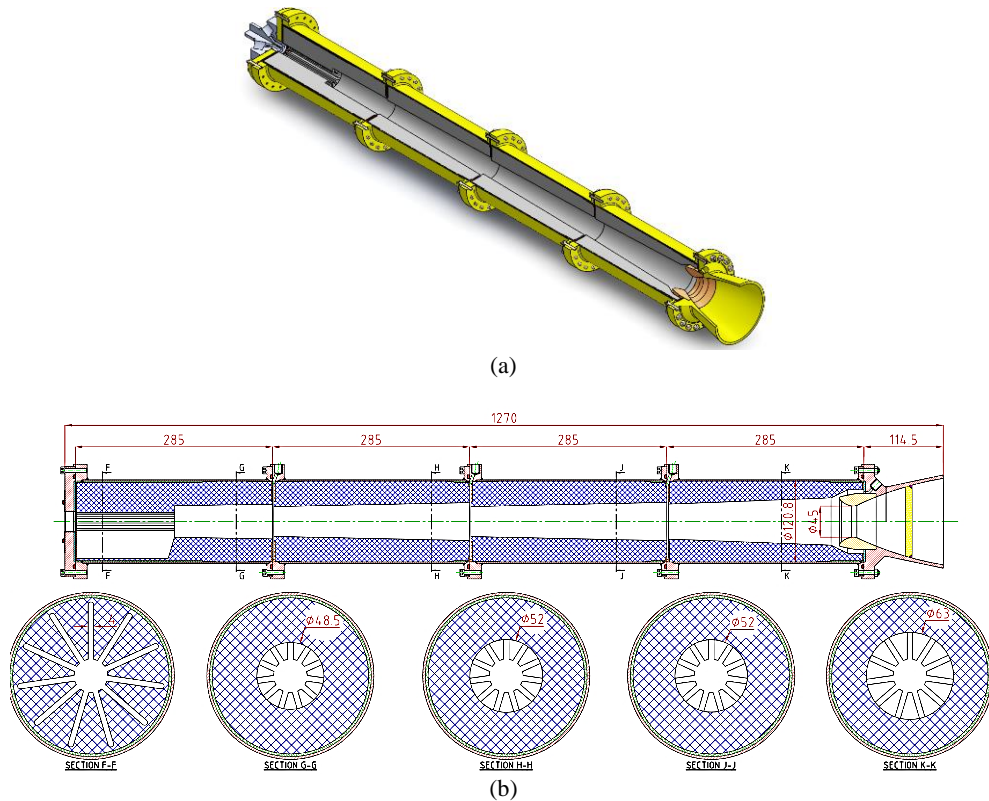


Fig. 6. RSRM subscale motor: a) 3D scheme, b) Dimensional scheme.

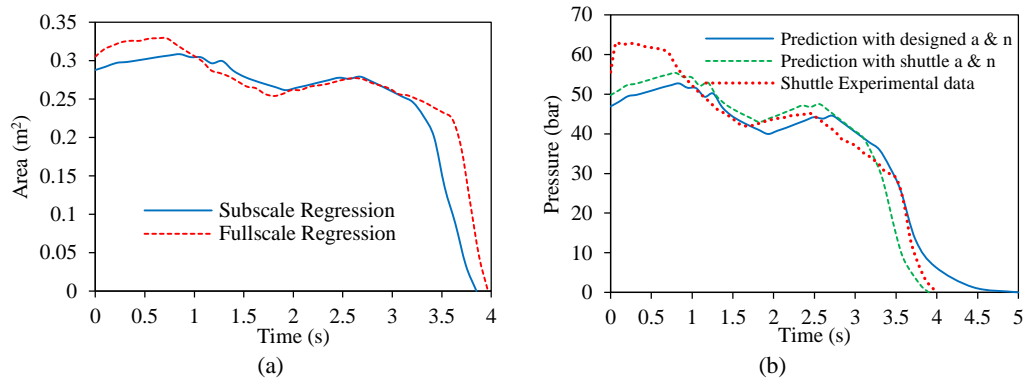


Fig. 7. Shuttle RSRM Full-scale & Subscale: a) Regression Comparison, b) Pressure Prediction.

applying \dot{r} definition and simplifying (Puskulcu & Ulas, 2008):

$$P = \left(\frac{a c^* \rho_p A_b}{A_t} \right)^{\frac{1}{1-n}} \quad (2)$$

Considering $a = 1.946$, $n = 0.405$, $d_t = 45 \text{ mm}$, $\rho_p = 1758 \text{ kg/m}^3$, $c^* = 1576$ and grain regression for A_b , the values of P respect to times are obtained accordance with Fig. 7(b).

4. ACOUSTIC COUPLING AND STROUHAL NUMBERS

Flow separation from the upstream inhibitor to downstream, as shown in Fig. 8 leads to coupling between vortex shedding and longitudinal acoustic

properties of the motor (Frezzotti, et al., 2018). First, four longitudinal acoustic frequencies of the motor can be determined using $f_{cc} = na/2L$ for a closed-closed chamber (Petersen & Murdock, 1990) with $L=1125 \text{ mm}$ and $a= 1065 \text{ m/s}$ like 474, 948, 1423 and 1897 Hz, respectively.

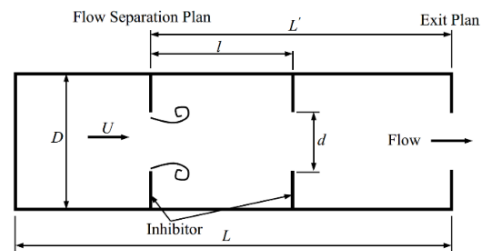


Fig. 8. Schema for a segmented motor chamber with two inhibitors.

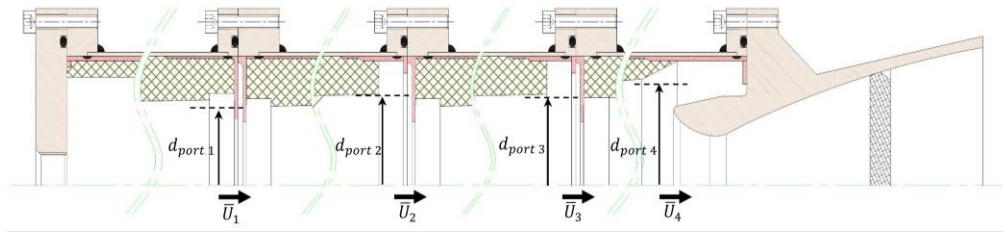


Fig. 9. Schematic of calculation position of mean flow velocity in sub-scaled motor.

The importance of the vortex impingement in the overall coupling seemed to have been overlooked and correlations were proposed through a Strouhal number defined as (Yadav, et al., 2015):

$$St_1 = \frac{fd}{U} \quad (3)$$

A value of St_1 of the order of or less than unity was considered as critical for the appearance of instabilities (Brown, et al., 1980). The physical mechanism behind vortex shedding is the instability of shear layers in the gas flow. For the present work, this analysis introduces a Strouhal number based on shear layer characteristics, such as its thickness δ , and the velocity difference across it ΔU_e :

$$St_2 = \frac{f\delta}{\Delta U_e} \quad (4)$$

The shear layer is unstable for a strouhal number in the range from 0 to 0.26 (Antoine, 2000). In a closed cavity, such as a solid propellant motor chamber, several other length scales should be taken into account and somewhat complicate the matter. First, there are the cavity dimensions, such as L and D , which govern the chamber acoustic mode frequencies and the mean flow velocity. Second, in closed cavities it is common to encounter a new length scale l characteristic of a standoff distance, in the direction of the mean velocity U , which is used to define a new Strouhal number as (Dular & Bachert, 2009):

$$St_3 = \frac{fl}{U} \quad (5)$$

Typical Strouhal numbers are about 0.1-1 (Petersen & Murdock, 1990). Strouhal numbers are about 4-12 when based on (3) and the axial velocity upstream of the first diaphragm. These values correspond to the range 1-3 when converted in terms of axial velocity just above the first diaphragm, indicating that at least one vortex has time to travel from one diaphragm to the other during an acoustic cycle (Vuillot, 1995).

4.1. Mean Flow Velocity

The gas velocity of solid propellant moves perpendicularly away from the burning surface. From the conservation law of mass, the injected gas velocity is obtained by (Blomshield1, 2007):

$$U_{inj} = \dot{r} \left(\frac{\rho_{propellant}}{\rho_{gas}} \right) \quad (6)$$

Now, calculation of mean flow velocity, \bar{U} , in various sections according to Fig. 9 is possible. As Regards the mass flow rate of each grain section is equal to the injection gas rate from the burning surface, conservation relation will be:

$$\begin{aligned} \dot{m}_{inj} = \dot{m}_{port} &\Rightarrow \rho_g A_b U_{inj} = \rho_g A_{port} \bar{U} \\ &\Rightarrow A_b U_{inj} = \pi \frac{d_{port}^2}{4} \bar{U} \\ &\Rightarrow \bar{U} = \frac{4A_b U_{inj}}{\pi d_{port}^2} \end{aligned} \quad (7)$$

From the above, the estimated analytical values of mean flow velocity will be obtained. Regarding availability of RSRM's mean flow velocity analytical values (Mason, et al., 2004), one can compare the results obtained with RSRM's values according to Fig. 10.

4.2. OVS Analysis

Experiments have shown that when aeroacoustic instability occurs, a number of vortices forms between the initiation and impingement points. The OVS frequency including of various flow parameters and the number of vortices between the vortex initiation point and the obstacle, m , is defined as (Dunlap, et al., 1990):

$$f_{ovs} \cong \frac{U_o}{l} \frac{(m - \alpha)}{(M_o + 1/k)} \quad (8)$$

where k and α are typically 0.58 and 0.25, respectively (Petersen & Murdock, 1990). The integer m is the mode or stage number with the value between 5-12 (Dotson & Sako, 2004). Comparing Eq. (4) with Eq. (8), a definition for the Strouhal number is obtained as (Petersen & Murdock, 1990):

$$St_{ovs} = \frac{f_{ovs} l}{U_o} = \frac{(m - \alpha)}{(M_o + 1/k)} \quad (9)$$

Applying Mach number values obtained from analysis and CFD in Eqs. (8) and (9), looking back to Fig. 9, the values of f_{ovs} and St_{ovs} will be obtained for positions one to four through the motor axis according to Fig. 11.

The shear layer is unstable for a Strouhal number in the range from 0 to 0.26. The maximum instability is obtained for $St_\delta = 0.05$. Using the Strouhal number definition based on momentum thickness (Wu & Kung, 2000):

$$St_\delta = \frac{f_{ovs} \delta}{\Delta U} \quad (10)$$

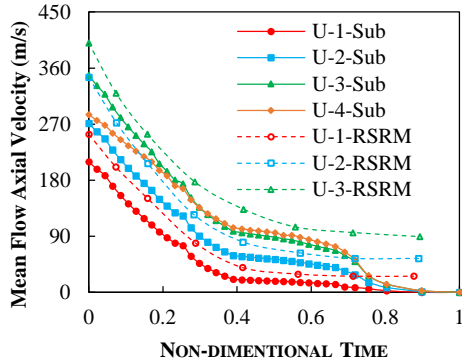
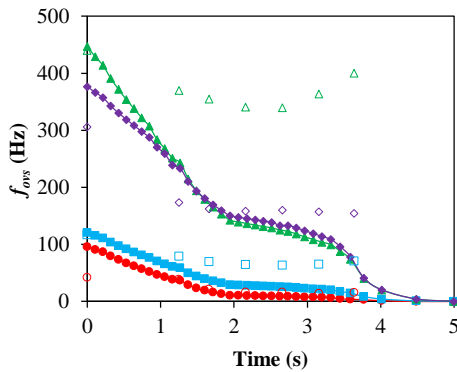
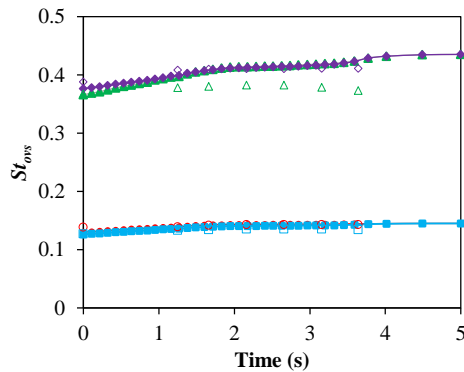


Fig. 10. Comparison of estimated analytical mean flow velocity obtained from sub-scaled motor and RSRM.



(a)



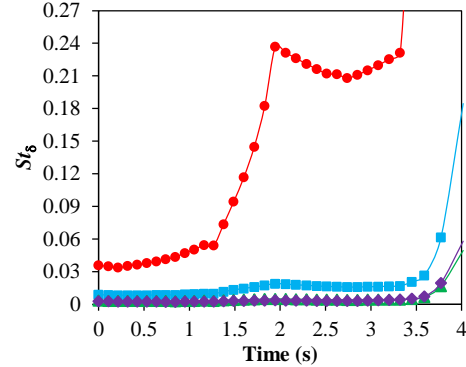
(b)

Fig. 11. Comparison of analysis (continuous line) and CFD (dashed line) results in positions of one (circles), two (rectangles), three (triangles) and four (diamonds) for: a) f_{ovs} and b) St_{ovs} .

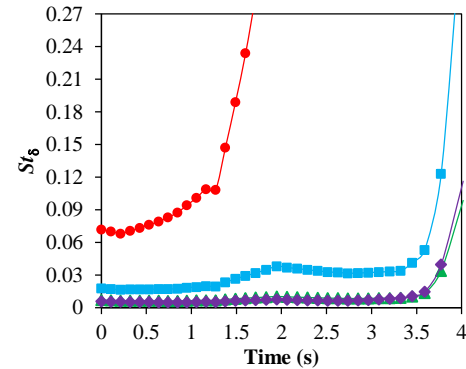
Strouhal number St_δ for the axisymmetric mode is between 0.015-0.017 (Michalke, 1971) One can finds after simplification that (Antoine, 2000):

$$\left(\frac{d}{D}\right)^{7/2} = \frac{\sqrt{8} St_\delta M_o^{3/2} L_r}{A n} \sqrt{\frac{L_r}{L}} \sqrt{\frac{aD}{v}} \quad (11)$$

Fig. 12 show the values of St_δ accordance with Eq. (11) in positions one to four through the motor axis for the first two modes.



(a)



(b)

Fig. 12. St_δ in positions of one (circles), two (rectangles), three (triangles) and four (diamonds) for a) first mode and b) second mode.

4.3. SVS Analysis

In a cylinder with lateral injection, SVS is related to the Taylor flow profile that may be unstable when the hydrodynamic frequency, f_h , is lower than the acoustic frequency, f_a . The hydrodynamic frequency can be obtained as (Ballereau, et al., 2006):

$$f_h = \frac{\Omega U_{inj}}{2\pi R_c} \quad (12)$$

For many composite propellants, omega value is between 5 and 30 (Blomshield1, 2007). Fig. 13 represents the f_h values for non-dimensional frequencies of 5 and 10 and its comparison with frequencies obtained from OVS calculation and CFD results.

4.4. AVS Analysis

Analysis of AVS criteria is difficult. Supposing a velocity profile that presents an inflection point exactly in the corner of the motor grain angle, the

Strouhal number St_{AVS} is defined as:

$$St_{AVS} = 2\pi \frac{faL_m}{U} \quad (13)$$

where $L_m \approx 0.8R_c$ is the thickness of the shearing layer. The criteria of AVS instabilities is $St_{AVS} < 1.7$ and its critical value can occur when $St_{AVS} = 0.3$ (Ballereau, *et al.*, 2006). Fig. 14 represent the St_{AVS} values for non-dimensional frequencies of 5 and 10 and its comparison with Strouhal number obtained from OVS calculation.

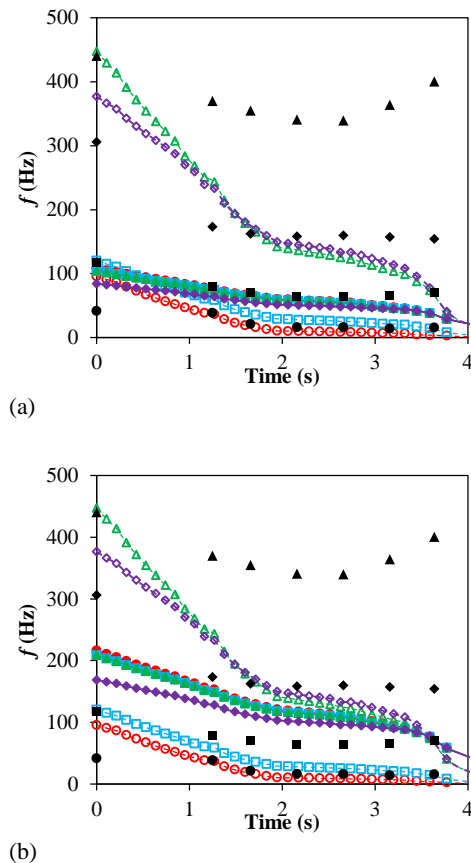


Fig. 13. Frequency comparison of analytical SVS (continuous line), analytical OVS (dashed line), and CFD (no line) results in positions of one (circles), two (rectangles), three (triangles) and four (diamonds) for a) $\Omega=5$ and b) $\Omega=10$.

5. FULL NUMERICAL APPROACHES

Full numerical approaches should be used, in providing unprecedented insight into oscillatory flow fields and become irreplaceable tools to predict motor stability, especially in geometrically complex situations (Stella & Pagila, 2011), (Fabignon, *et al.*, 2003). To this end, the 2D flow has been solved using the computational fluid dynamics software “ANSYS-FLUENT”, due to its good capability and user-friendliness (Kostić, *et al.*, 2015).

For CFD analysis of the present work, combustion was not considered (Anthoine, *et al.*, 2000). The flow was assumed hot, 2D axisymmetric, viscous flow,

ideal gas and uniform injection of fluid normal to the boundary (Zhao, *et al.*, 2018). The $k-\omega$ SST model was used to model turbulence effects (Praveen laws & Lakshmiganthan, 2013). Despite using transient solution is better and more accurate (Zhao, *et al.*, 2018), steady state method was used due to author’s limitation on calculation space and this is a desirable approach used in some references.

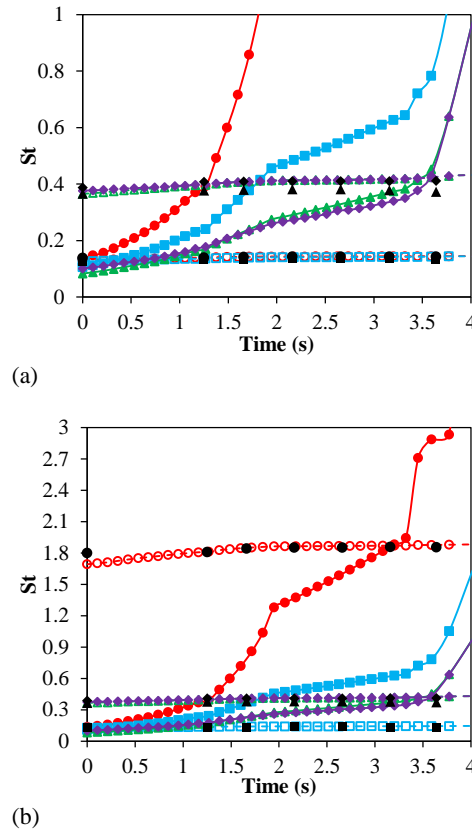


Fig. 14. Strouhal comparison of analytical AVS (continuous line), analytical OVS (dashed line), and CFD (no line) results in positions of one (circles), two (rectangles), three (triangles) and four (diamonds) for a) $\Omega=5$ and b) $\Omega=10$.

The time step and convergence criterion were set to 10^{-4} s and 10^{-6} , respectively. Under-Relaxation Factors include turbulence kinetic energy, dissipation rate, viscosity, and Courant number, were set as 0.8, 0.8, 1 and 10, respectively. Discretization Equation includes the gradient, flow, turbulence kinetic energy, and dissipations rate, was selected as least square cell-based and second-order upwind, respectively.

The properties of gas include of specific heat, thermal conductivity, viscosity, and molecular weight were taken as 1901 J/Kg.°K, 0.034 W/m.°K, 9×10^{-5} Kg/m.s and 28.23 Kg/Kmol, respectively. The shape of the thermal inhibitor between segments of propellant can be taken either rigid (Kourta & Soula, 1995) or flexible (Richard *et al.* 2007). In this project, the shape of frontal thermal inhibitors is assumed rigid with considering ablation in definite modeling time. As shown in Fig. 15, pressure and

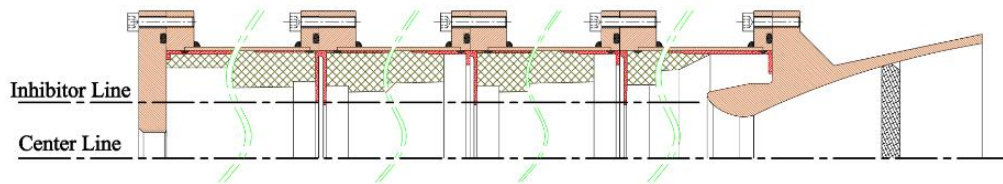


Fig. 15. Measurement position of pressure and velocity data from CFD in center line and inhibitor line.

velocity data have been taken in two positions of the centerline and inhibitor line.

Evaluation of grid sensitivity (Lee, *et al.*, 2017) was done to obtain acceptable results in CFD including 21000, 41000 and 64000 grids. As shown in Fig. 16, the difference of Mach number results between 21000 and 41000 grids is obvious with the maximum error of 93%, but when grid became finer to 64000 grids, this difference, nearly, eliminated with the maximum error of 8.9%. The value of Y^+ for this grid was less than 30 indicating the good resolution of the boundary layer (Abdul Raheem & Babu, 2004).

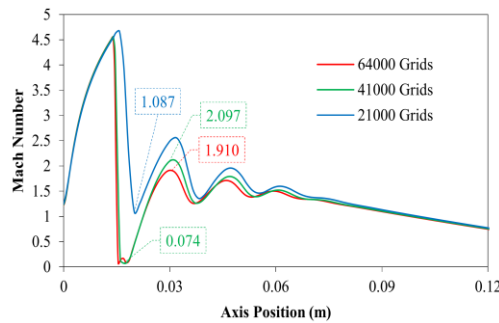


Fig. 16. Evaluation of Grid Resolution on CFD Results.

Fig. 17 to Fig. 18 represent streamline contours. Briefly, only CFD results of some interesting contours have been shown. Fig. 19 represents the comparison between CFD solutions for pressure in axis and inhibitor line of the motor for various regression times.

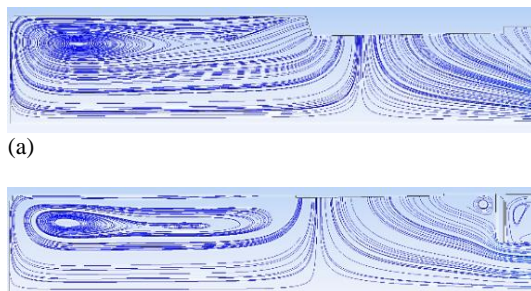


Fig. 17. Stream line in segment 1; a) $t=2.66$ s, b) $t=3.64$ s.

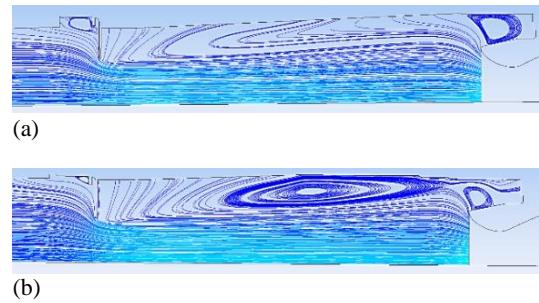


Fig. 18. Stream line in segment 4; a) $t=2.66$ s, b) $t=3.16$ s.

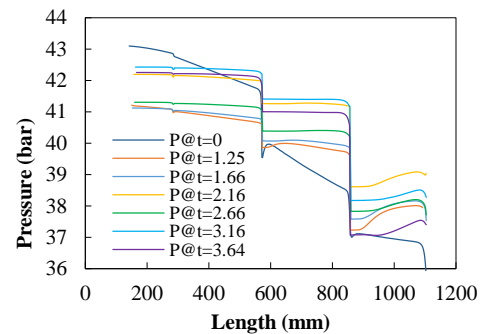
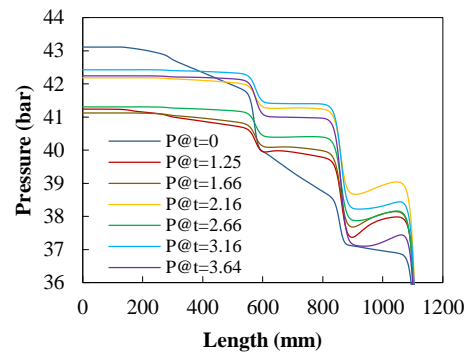


Fig. 19. Comparison of CFD temporal pressure data in a) center line, b) inhibitor line.

6. STATIC TEST AND DATA ACQUISITION

Each of the sub-scaled RSRMs was static tested in a horizontal configuration, as shown in Fig. 20. The test stand was mounted on a concrete test bed having a thrust wall. The head end of the motor was connected to a 5000 N load cell, concentric to the longitudinal axis of the motor. Instrumentation consisted of two piezoelectric Kistler 701 pressure

transducers applied in positions two ($z=570$ mm) and three ($z=855$ mm).

Pressure signals were split into two channels consisting of a total signal and of a band pass filtered signal. Each output of load cell and pressure transducers were provided with separate power supply, cables, amplifiers, and data acquisition system to have complete redundancy. Avoiding the vibration and sound level in the instrumentation room due to the firing of the rocket motor, the preamplifiers were required.

Data acquisition was performed through an A/D converter at a 2 kHz sampling rate per channel and started 10 s prior to ignition. The pressure time plots of one of the sub-scaled RSRM and its comparison with prediction have been shown in Fig. 21. Fig. 22 represents the pressure time history of two motor different positions, obtained from CFD and its comparison with shuttle prediction and test data. The configuration of thermal protection inhibitors before and after the static test has shown in Fig. 23.

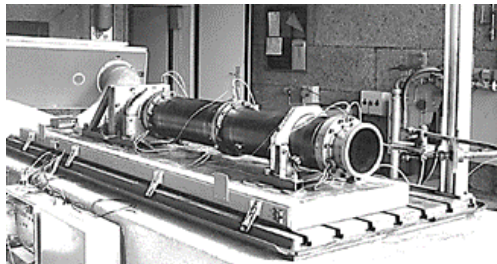


Fig. 20. Test stand used for firing of sub scaled motor.

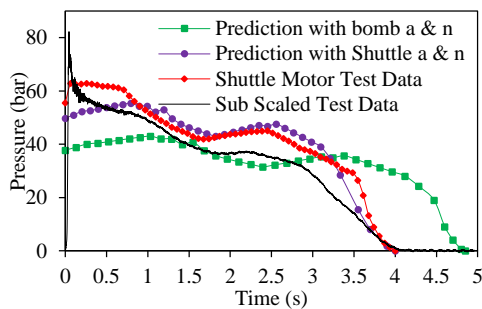


Fig. 21. Pressure result of sub-scaled static test and comparison with prediction.

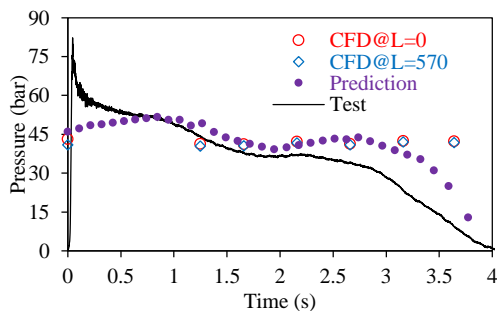


Fig. 22. Comparison of pressure data obtained from CFD, prediction and test.

The amplitude of pressure oscillations respect to time and FFT has been calculated from experimental pressure data using a code-named “POA” that has been written by the authors. Briefly, the programming language and its graphical interface are C# and Visual Studio Software, respectively. The code, at first, loads discrete data of pressure versus time obtained from test and then identifies point-to-point maximum and minimum pressures relative to mean pressure.

Pressure oscillation result of each sensor position and acquisition noise have been shown in Fig. 24. To understand the characteristics of the oscillations in different time duration and sensing position on the motor, Fig. 25 shows a detailed view at time intervals 0-0.4. The FFT analysis has been carried out for test pressure oscillations data and represented in Fig. 26 and Fig. 27 for positions $z=570$ mm and $z=855$ mm, respectively. Comparison of pressure oscillations versus non-dimensional time between subscale and full-scale RSRM has shown in Fig. 28.



(a)



(b)

Fig. 23. Thermal protection inhibitor rings; a) before test, b) after test.

1. DISCUSSION

As shown in Fig. 11(a), the values of OVS frequencies both in analysis and CFD are close to each other. These values in positions one and two (forward and forward centered segments) are about 100 Hz, but interestingly, in positions three and four (aft centered and aft segments), an increase is observed. This shows that, most probably, with approaching to the nozzle, vortex shedding due to OVS is increasing. This claim is confirmed by St_{OVS} calculations. According to that mentioned previously, $St_{OVS} < 1$ is equal to the existence of OVS vortex shedding. From Fig. 11(b), Strouhal number obtained from analysis and CFD, in all

segments is less than one and so confirms the existence of OVS vortex shedding.

As mentioned above, the shear layer is unstable for a St_δ in about zero to 0.26 and maximum instability is obtained for $St_\delta=0.05$. Fig. 12(a) and (b) show that St_δ of all positions for two first modes (except

forward segment) approximately in all burning time is less than 0.02 and represents that shear layer exists in these positions. St_δ of position two is near to positions three and four but the difference in higher modes becomes large and so the shear layer effect in

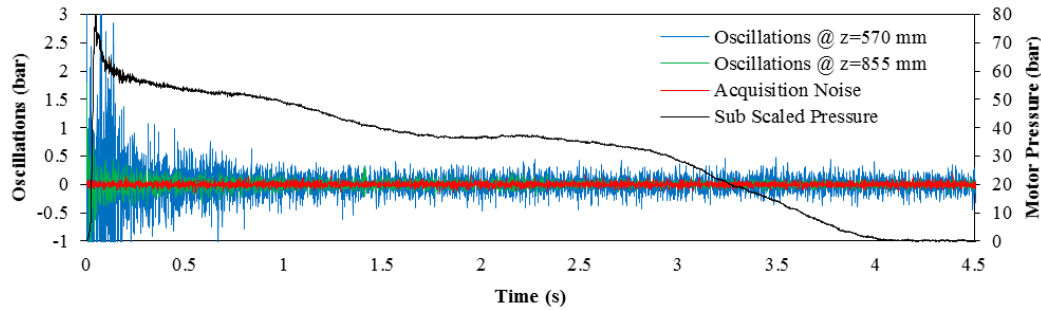


Fig. 24. Oscillation result of sub-scaled static test and its oscillations in different positions.

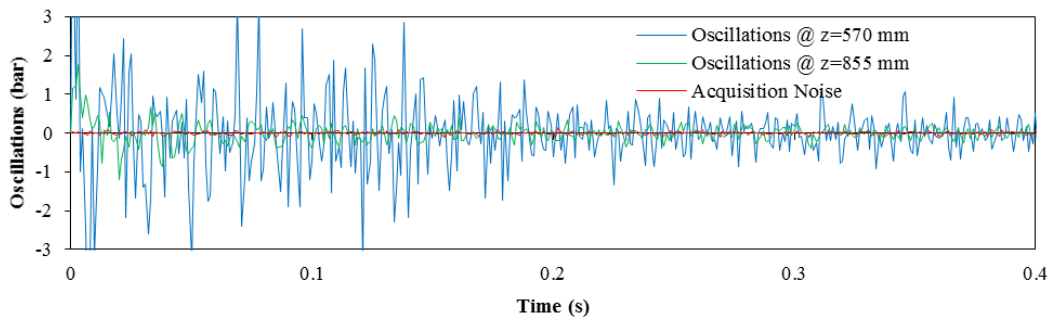


Fig. 25. Comparison of sub-scaled pressure oscillations in different positions at time=0-0.4 s.

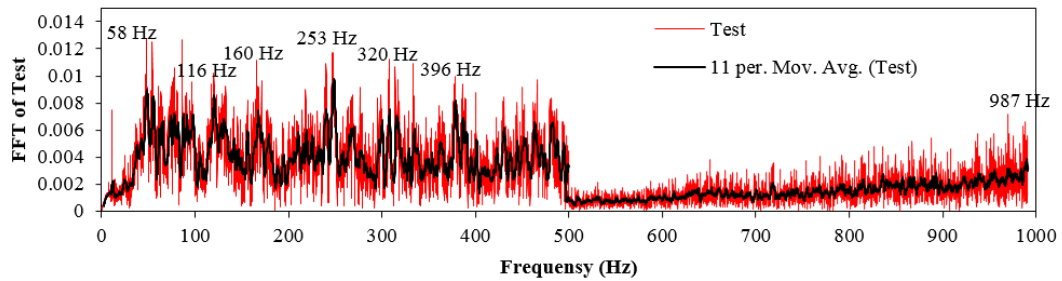


Fig. 26. FFT of Experimental Results at $z=570$ mm.

this position decreased with time. Although St_δ of position one is higher than other positions and has a progressive steeper slope, this value for the first and second modes is less than 0.26 until $t\sim 3.5$ s and $t\sim 2$ s, respectively. Therefore, it seems that shear layer effects are not, really, important in this position.

Fig. 13(a) and (b) show that f_h in all positions is less than the first acoustic mode ($f_{a_1} = 474$ Hz) and so these positions are capable of vortex shedding due to SVS. Fig. 14 shows that St_{AVS} in all positions of 1 to 4 is less than 1.7 and so these positions are capable of vortex shedding due to AVS. It seems that in the presented sub-scaled motor, dominant Strouhal number is St_{OVS} .

In all evaluated mean pressure curves using fluent, it is observed that the pressure decreases with a smooth

and immediately slope in the separation position of segments on the motor axis and inhibitor line, respectively. Similar behavior, but with a few differences is observed on mean velocity curves. Flow turning and vortex shedding is observed at time $t=1.25$ s in streamlines contours on the end segment of the motor. In addition, negative velocity in the separation position of segments is observed. At time $t=1.66$ s, vortex and negative velocity are not observed. At time $t=2.16$ s, vortex formation is obvious on streamlines for first, middle and end segments of the motor. At time $t=2.66$ to $t=3.64$, vortex form becomes gradually bigger in the first segment and is observed in the submerged hole and the gaps between segments (as shown in Fig. 17 and Fig. 18). In this interval, negative velocity exists.

As represented in Fig. 19, the pattern of pressure

reduction with respect to motor length in overall time is the same, expect initiate time. Among reasons that can be referred in justification of difference between the pattern of pressure in initiating time and other times is that in motor initiating time, cylindrical shape of grain has been yet preserved and no step or large gap formed between segments.

As shown in Fig. 21, action time prediction with shuttle propellant properties and those obtained from Crawford bomb differs. Therefore, despite using Buckingham's Pi-theorem in solid motor scaling, propellant chemistry and its burning rate are affected of Crawford bomb and real flow of combustion

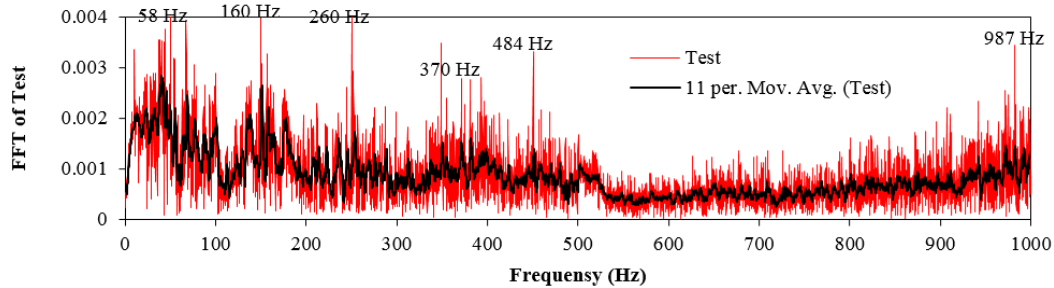


Fig. 27. FFT of Experimental Results at $z=885$ mm.

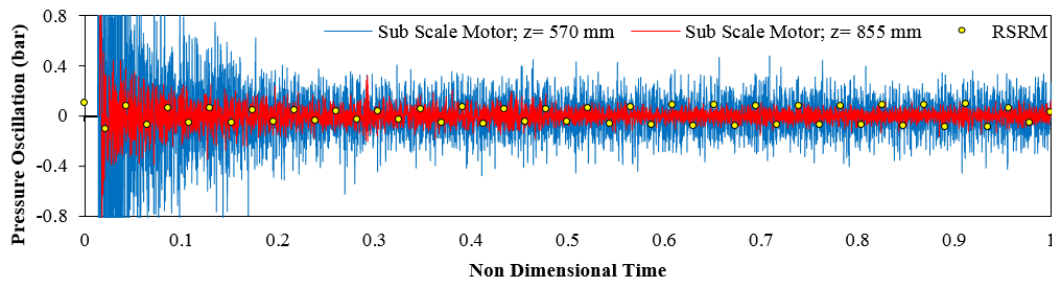


Fig. 28. Comparison of pressure oscillation between subscale motor and RSRM.

products and in many cases, error correction between Crawford and motor data is inevitable. As shown in Fig. 22, pressure data obtained from CFD has a good agreement with prediction but a few differences are observed with test data.

The configuration of thermal protection inhibitors before and after the static test, as shown in Fig. 23, demonstrates that a considerable amount of inhibitor material has remained and indicates that the existence of the vortex shedding phenomenon is inevitable. According to pressure data from the static test, the peak-to-peak amplitude of the oscillations is between 0.4 to 1.2 bar and so 1% to 3% of the mean chamber pressure.

Comparison between test data (Fig. 24 and Fig. 25) and CFD results (Fig. 19) shows that pressure level in $z=570$ mm is higher than $z= 855$ mm and so pressure oscillations have the same behavior.

Looking up to test data FFT, as represented in Fig. 26 and Fig. 27, demonstrates that not only first and second acoustic frequencies (474 Hz and 948 Hz, respectively) are subjected to excite, but also some smaller frequencies like 58, 116, 160 and 253 Hz are excited. Comparison between Fig. 26 and Fig. 27 shows that the amplitude of oscillations in the distance $z=570$ mm from the motor's head end is higher than $z=885$ mm and indicates that the power of vortex shedding in the middle of the motor is more significant. In addition, there are dominant

frequencies between 100 to 500 Hz. Let us look at the OVS frequency's curves in Fig. 11(a). Although the frequencies about 450 to 500 Hz are only due to OVS in positions three and four in the initial time of the motor burning, comparison of this figure with Fig. 13 shows that the lower frequencies about 100 to 200 Hz are due to both the OVS and SVS in the total time of the motor burning.

As shown in Fig. 28, oscillations amplitude at $z=855$ mm has a good agreement with RSRM data. Of course, there is no information about the position of pressure transducers of RSRM.

2. CONCLUSIONS

The analysis relations, CFD simulation and static test results of a sub-scaled RSRM for evaluation of vortex shedding driven oscillations have been presented. Evidently, simple methods are available to give valuable information on the existence of aeroacoustic pressure oscillations. These methods are essential to understanding the mechanisms of vortex shedding and aeroacoustic coupling. Computational fluid dynamics have been shown to be very useful in providing insight into oscillatory flow fields especially in geometrically complex grain configurations. Results show that various definitions for Strouhal number are useful only for primarily glance on vortex shedding and pressure oscillations and so CFD solution and test program are inevitable

for a correct understanding of the ballistic operational condition of the motor. In addition, despite aggress of pressure test data and grain-burning regression of sub-scaled motor to full-scale motor, internal flow phenomenon may be different due to small-scale time and dimension with the full-scale motor. The FFT plots show that only one dominating peak and a few low secondary peaks have been noted. The fluctuation is irregular. Data obtained from Sub-scaled RSRMs during static testing showed unanticipated small amplitude oscillations in both pressure and thrust. As the frequency and the duration of the oscillations occurring in both the pressure and thrust are more or less same, the phenomena are probably due to combustion process and the configuration of the propellant grain in the segmented motors.

REFERENCES

- Abdul Raheem, S. and V. Babu (2004). *Numerical Simulations Of Unsteady Flows In Solid Rocket Motors*. s.l., American Institute of Aeronautics and Astronautics.
- Anthoine, J., D. Yildiz and J. M. Buchlin (2000). *Nozzle Design Effect On Vortex Induced Instabilities In An Axial Injected Cold Flow Model of The Ariane-5 EAP*. Nice, France, s.n.
- Antoine, J. (2000). *Experimental And Numerical Study of Aero Acoustic Phenomena in Large Solid Propellant Boosters*, Bruxelles: University of Libre De Bruxelles.
- Ballereau, S., F. Godfroy, O. Orlandi and D. Ballion (2006). *Numerical Simulations and Searching Methods of Thrust Oscillations for Solid Rocket Boosters*. Sacramento, California, American Institute of Aeronautics and Astronautics.
- Blomshield1, F. S. (2007). *Lessons Learned In Solid Rocket Combustion Instability*. Cincinnati, OH, American Institute of Aeronautics and Astronautics.
- Brown, R. S., R. Dunlap, S. W. Young and R. C. Waugh, (1980). *Vortex Shedding as an Additional Source of Acoustic Energy in Segmented Solid Propellant Rocket Motors*. Hartford, American Institute of Aeronautics and Astronautics.
- Cosyn, P., J. Vierendeels and J. Anthoine (2005). Numerical Simulation of Aeroacoustic Phenomena in a Solid Rocket Booster. *Journal Of Spacecraft And Rockets*, 42(1), 111-117.
- Culick, F. E. (2006). *Unsteady Motions in Combustion Chambers for Propulsion Systems*, s.l.: North Atlantic Treaty Organisation.
- Dotson, K. W., S. Koshigoe and K. K. Pace (1997). Vortex Shedding in a Large Solid Rocket Motor Without Inhibitors at the Segment Interfaces. *Journal Of Propulsion and Power*, March – April, 13(2), 197-206.
- Dotson, K. W. and B. H. Sako (2004). *An Investigation of Propulsion-Structure Interaction in Solid Rocket Motors*. Los Angeles, American Institute of Aeronautics and Astronautics.
- Dular, M. and R. Bachert (2009). The Issue of Strouhal Number Definition in Cavitating Flow. *Journal of Mechanical Engineering*, 55(11), 666-674.
- Dunlap, R. Blackner, A. M., Waugh, R. C., R. C. Brown and P. G. Willoughby (1990). Internal Flow Field Studies in a Simulated Cylindrical Port Rocket Chamber. *Propulsion* 6(6), 690-704.
- Fabignon, Y. V. J. Dupays, G. Avalon, F. Vuillot, N. Lupoglazoff, G. Casalis and M. Prévost (2003). Instabilities and pressure oscillations in solid rocket motors. *Aerospace Science and Technology*, 7, 191-200.
- Ferretti, V. B. Favini, E. Cavallini, F. Serraglia and M. D. Giacinto (2011). *Pressure oscillations simulation in P80 SRM first stage VEGA launcher*. San Diego, American Institute of Aeronautics and Astronautics.
- Ferretti, V. B. Favini, E. Cavallini, F. Serraglia and M. D. Giacinto (2011). *Vortex-sound Generated Pressure Oscillations Simulation in Internal Flow by means of Q-1D Model*. Rome, EUCASS.
- Flandro, G. A., S. R. Fischbach and J. Majdalani (2007). Nonlinear rocket motor stability prediction: Limit amplitude, triggering and mean pressure shift. *Physics of Fluids* 19(094101).
- Frezzotti, M. L. et al. (2018). Quasi-1D modeling of heat release for the study of longitudinal combustion instability. *Aerospace Science and Technology*, April 75, 261-270.
- Golafshani, M. and H. T. Loh (1989). *Computation of Two-Phase Viscous Flow in Solid Rocket Motors Using a Flux-Split Eulerian-Lagrangian Technique*. Monterey, American Institute of Aeronautics and Astronautics.
- Guéry, J. F. S. Ballereau, F. Godfroy, S. Gallier, O. Orlandi and P. D. Pieta (2008). *Thrust Oscillations in Solid Rocket Motors*. Hartford, CT, American Institute of Aeronautics and Astronautics.
- Isakari, S. Asakura, D. Haraguchi, Y. Yano and A. Kakami (2017). Performance evaluation and thermography of solid-propellant microthrusters with laser-based throttling. *Aerospace Science and Technology* 71, 99-108.
- Javed, A. and D. Chakraborty (2015). Universal erosive burning model performance for solid rocket motor internal ballistics. *Aerospace Science and Technology* 45, 150-153.
- Kostić, O. P., Z. A. Stefanović and I. A. Kostić (2015). CFD Modeling of Supersonic Airflow Generated by 2D Nozzle With and Without an

- Obstacle at the Exit Section. *FME Transactions* 403, 107-113.
- Kourta, A. (1996). Vortex Shedding in Segmented Solid Rocket Motors. *Journal of Propulsion and Power* 12(2), 371-376.
- Kourta, A. and C. Soula (1995). *Vortex Shedding in Solid Rocket Motors*. Reno, American Institute of Aeronautics and Astronautics.
- Lee, K., S. Heo, S. Kwon and J. Lee (2017). A study on the unsteady conjugate heat transfer of hot gas valve. *Aerospace Science and Technology*, September 68, 362-369.
- Lee, S., D. Y. Kim and C. Lee (2017). The frequency characteristics of the shear layer oscillation in hybrid rocket post-chamber. *Aerospace Science and Technology* 70, 388-395.
- Mason, D. R., S. L. Folkman and M. A. Behring (1979). *Thrust Oscillations Of The Space Shuttle Solid Rocket Booster Motor During Sta'pic Tests*. Las Vegas, Nevada, American Institute of Aeronautics and Astronautics.
- Mason, D. R. *et al.* (2004). Pressure Oscillations and Structural Vibrations in Space Shuttle RSRM and ETM-3 Motors.
- McWhorter, B. B., M. E. Ewing, D. E. Bolton, K. U. Albrechtsen, T. E. Earnest, T. C. Noble and M. Longaker (2003). *Real-Time Inhibitor Recession Measurements In Two Space Shuttle Reusable Solid Rocket Motors*. Huntsville, Alabama, AIAA.
- Michalke, A. (1971). *The Instability Of Free Shear Layers*, Berlin: s.n.
- Petersen, E. L. and J. W. Murdock (1990). *Active Control of Vortex-Driven Oscillations in a Solid Rocket Motor Using a Cold-Flow Simulation*. Reno, American Institute of Aeronautics and Astronautics.
- Praveen laws, L. G. and S. M. Lakshminathan (2013). Numerical Simulations of Combustion Instability and Pressure Oscillation in Solid Rocket Motor. *International Journal of Engineering Research & Technology (IJERT)*, November 2(11), 2961-2966.
- Prévost, M., J. C. Godon and O. Innegraeve (2005). *Thrust Oscillations in reduced Scale Solid Rocket Motors, part I: Experimental Investigations*. Tucson, Arizona, American Institute of Aeronautics and Astronautics.
- Puskulcu, G. and A. Ulas (2008). 3-D grain burnback analysis of solid propellant rocket motors: Part 1 – ballistic motor tests. *Aerospace Science and Technology* 12(8), 579-584.
- Richard, J., T. Morel and F. Nicoud (2007). *Effect of the Fluid-Structure Interaction on Solid Rocket Motors Instabilities*, Montpellier, France: s.n.
- Seifollahzadeh, A. and A. Aminian (2014). Simulation and Study of the Effect of Pressure Oscillations on Linear Combustion Instability in a Double Base Solid Rocket Motor. *Chemical Engineering & Process Technology* 5(2).
- Stella, F. and F. Pagila (2011). Pressure oscillations in solid rocket motors: Numerical study. *Aerospace Science and Technology*, January–February 15(1), 53-59.
- Thirumoorthy, M., S. R. Chakravarthy and P. V. Brahmaandam (2017). Shape effects of single axisymmetric cavity in a circular duct on flow induced acoustic oscillations. *Aerospace Science and Technology* 67, 181-192.
- Traineau, J. C. M. Prevost, F. Vuillot, P. L. Breton, J. Cuny, N. Preioni and R. Bee (1997). A Subscale Test Program to Assess the Vortex Shedding Driven Instabilities in Segmented Solid Rocket Motors. *AIAA*.
- Vuillot, F. (1995). Vortex-Shedding Phenomena in Solid Rocket Motors. *Journal Of Propulsion And Power* 11(4), 626-639.
- Wu, W. J. and Kung, L. C. (2000). Determination of Triggering Condition of Vortex-Driven Acoustic Combustion Instability in Rocket Motors. *Journal of Propulsion And Power*, November–December, 16(6), 1022-1029.
- Yadav, D., R. Srivastava and J. Lee (2015). Numerical Simulation of Vortex Shedding Past a Single Cylinder Confined in a Channel. *Fluid Mechanics*, 1(1), 1-4.
- Zhao, B. N. Yu, Y. Liu, P. Zeng and J. Wang (2018). Unsteady simulation and experimental study of hydrogen peroxide throttleable catalyst hybrid rocket motor. *Aerospace Science and Technology* 27-36.
- Zhao, X., Z.-X. Xia, B. Liu, Z. Lv and L. k. Ma (2018). Numerical study on solid-fuel scramjet combustor with fuel-rich hot gas. *Aerospace Science and Technology* 77, 25-33.